

Autonomous Lunar Orbit Determination using Star Occultation Measurements

Mark L. Psiaki* and Joanna C. Hinks†
Cornell University, Ithaca, N.Y. 14853-7501

A method has been developed for performing autonomous Lunar orbit determination based on measurements of the times at which stars set behind or rise above the Lunar limb. This system is being developed as a possible technology for use in the Lunar exploration initiative because it enables increased autonomy of operations near the Moon. The system consists of a specially modified star camera and an extended Kalman filter. The star camera keeps track of known stars in its field of view and reports the times when stars suddenly appear or disappear without crossing the edge of the field of view. These are times that the known line-of-sight vectors to the stars cross the Lunar limb, and this knowledge translates into position information. The Kalman filter uses a series of star occultation/rising times and an orbital dynamics model to estimate the spacecraft's position and velocity. An observability analysis shows that this system is strongly observable, and a truth-model simulation has demonstrated an absolute position accuracy of 70 m per axis and an absolute velocity accuracy of 0.045 m/s per axis when using a Lunar topographic map with an RMS altitude accuracy of 100 m and a Lunar gravity model with an RMS accuracy of 1×10^{-5} m/s².

I. Introduction

THE current NASA initiative to explore the Moon has given rise to a renewed impetus for developing techniques for spacecraft operations in the Moon's vicinity. One useful technology would be an ability to do autonomous orbit determination for Lunar-orbiting satellites. Such an ability could reduce the cost of operations and enhance their reliability through elimination of the need for attention from Earth-based tracking stations. The usefulness of autonomy has been recognized in ¹, which proposes a means to achieve autonomous orbit determination for a pair of spacecraft, one a Lunar orbiter and the other located in a halo orbit about the L₂ Lunar libration point.

The present paper defines and analyzes another type of autonomous orbit determination method that is appropriate for use in Lunar orbits. It estimates a spacecraft's orbit based on measurements of the times when stars are occulted behind the Lunar limb or rise above it. This measurement concept is illustrated in Fig. 1. Each such measurement places the spacecraft on a surface that is roughly conical; its vertex is at the star, and its sides are tangent to the Moon's surface. The large distance of any star from the Moon causes this surface to be more like a cylinder whose axis is parallel to the known direction to the star and whose location and diameter make the cylinder tangent to the Moon. Six such measurements, if geometrically independent, should suffice to determine the six elements of a spacecraft's orbit about the Moon.

There already exist autonomous orbit determination concepts that employ a star sensor. A survey of early work on autonomous orbit determination is contained in ². This survey discusses the idea known as the space sextant, in which autonomous orbit determination is accomplished by using an estimator that operates on measurements of the nadir direction and of the directions to stars. Similar ideas that use bearing measurements to celestial bodies are contained in ^{3,4}. The star occultation measurement proposed here has already been suggested ^{5,6}, but most past work focused on Earth-orbiting satellites. Such a system is not likely to perform well for Earth orbits because of the large uncertainties in occultation/rising height due to the variable effects of the Earth's atmosphere. Several previous analyses concentrated on addressing and overcoming these uncertainties ^{7,8,9,10}. An experiment performed on the Gemini X mission found Earth orbit errors of about 1.8 km RMS ¹¹. One study, involving simulation of a

* Professor, Sibley School of Mechanical and Aerospace Engineering, 206 Upson Hall. Associate Fellow, AIAA.

† Graduate Student, Sibley School of Mechanical and Aerospace Engineering.

circumlunar mission with occultations by both the Earth and Moon, reported final position errors of one or more miles ¹².

Two of the principal error sources that degrade the performance of a star occultation system are uncertainty in Lunar topographic maps and uncertainty in Lunar gravity field models. Topography uncertainties lead directly to uncertainty in the position information that is contained in the measurement. Gravity model uncertainty degrades

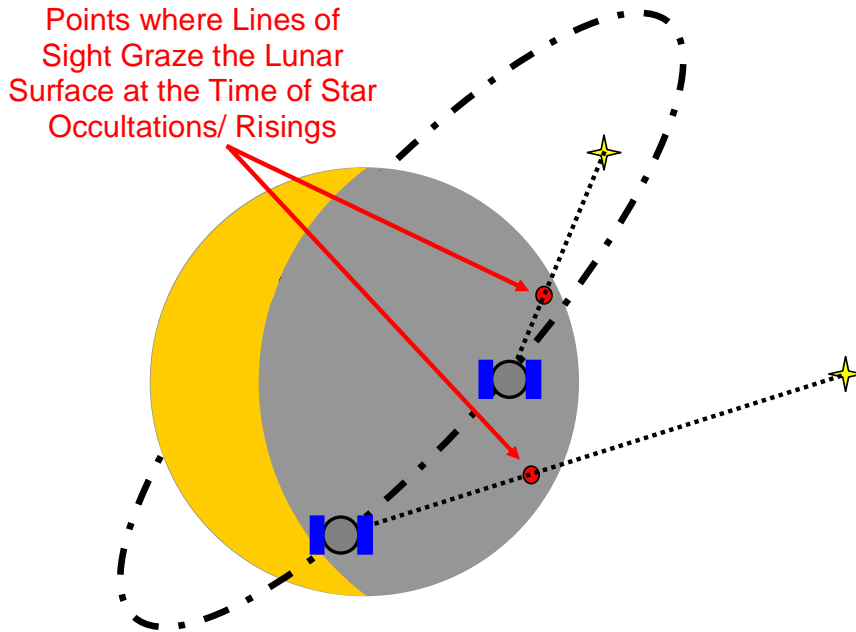


Figure 1. Illustration of two star occultation/rising measurements along a spacecraft's Lunar orbit.

the accuracy of the dynamic propagation phases, which are needed in order to string together the multiple measurements required to fully determine an orbit.

The proposed system has the potential to achieve much better accuracy than any of the predecessor star-based autonomous orbit determination systems. Occultation/rising measurements provide much better locational precision than do the measurements used in other concepts. Most previous work using occultation measurements for orbit determination did not employ Kalman filtering techniques because the method was not very widely known or applied when the studies were conducted. By using only Lunar (as opposed

to Earth) occultations, the new system avoids atmospheric uncertainty as a source of error, and other uncertainties (such as Lunar topography and gravity) are known to much greater accuracies presently than when the previous occultation studies were performed.

The current emphasis on Lunar exploration has given rise to several missions that are likely to improve knowledge of the Moon's topography and gravity field. The Japanese mission SELENOlogical and ENgineering Explorer (SELENE), which was scheduled for an August 16, 2007 launch but was postponed, will map the Moon's gravity field ¹³. The Lunar Reconnaissance Orbiter mission will carry a laser altimeter that will be used to map the Moon's topography with 1 m RMS errors on a 100 m grid resolution, and this instrument may also be used for orbit determination and gravity model refinement ¹⁴. The expected improvements in knowledge of the Moon's geographic shape and gravity field will serve to improve the potential accuracy of this paper's autonomous orbit determination method.

The five contributions of this paper are as follows: First, it develops a dynamics model and a measurement model for use in an autonomous orbit determination extended Kalman filter (EKF) that is based on star occultation/rising measurements. Second, it explores the error sources in these measurements. Third, it implements an EKF based on the developed models. Fourth, it develops and performs a linearized observability/constructability analysis of the proposed system. Fifth, it applies its EKF to data from a truth-model simulation in order to determine the system's expected performance.

This paper describes its models, its Kalman filter, and its observability and truth-model simulation studies in four main sections plus conclusions. Section II develops the system's dynamics model and measurement model, and it analyzes the error sources in the measurement model. Section III applies the extended form of the Square-Root Information Filter (SRIF) in order to create an algorithm for estimating the spacecraft orbit from the occultation/rising measurements. The SRIF is specially tailored to deal with the possibility that a batch of star occultation/rising measurements will be distributed over a single filter sample interval. This section also explains how to perform a linearized observability calculation for the system. Section IV documents the truth-model

simulation whose data have been used to test the filter's performance. Section V discusses the results of the observability analysis and the results of the filter performance tests. A summary and conclusions are presented in Section VI.

II. Models of Orbital Dynamics and Star Occultation/Rising Measurements

This section defines the state vector, the orbital dynamics model, and the star occultation measurement model that are used in the Lunar orbit determination filter. It also analyzes the proposed measurement model and suggests possible enhancements. The state vector and the dynamics model borrow heavily from the model in ¹⁵ and are presented here only in a brief summary form.

A. State Vector and Dynamics Model

The Lunar orbit determination Kalman filter uses the following 10-dimensional state vector:

$$\mathbf{x} = [\mathbf{r}^T, \mathbf{v}^T, \delta\mathbf{a}^T, \beta]^T \quad (1)$$

where \mathbf{r} is the spacecraft Cartesian position vector in Moon-Centered, Inertially-Fixed (MCIF) coordinates, \mathbf{v} is the spacecraft Cartesian velocity vector in MCIF coordinates, $\delta\mathbf{a}$ is a disturbance acceleration vector in MCIF coordinates, and β is a solar radiation pressure coefficient. The dimensional units of β are area divided by mass.

The position and velocity of the spacecraft evolve according to the usual laws of dynamics under the assumption that the only forces are gravity, solar radiation pressure, and the forces that cause the disturbance acceleration $\delta\mathbf{a}$. The first-order nonlinear equations that describe this motion are:

$$\begin{bmatrix} \dot{\mathbf{r}} \\ \dot{\mathbf{v}} \end{bmatrix} = \begin{bmatrix} \mathbf{v} \\ \mathbf{g}(\mathbf{r}, t) + \delta\mathbf{a} + \beta p_s(\|\mathbf{r} - \mathbf{r}_s\|)(\mathbf{r} - \mathbf{r}_s) / \|\mathbf{r} - \mathbf{r}_s\|^3 \end{bmatrix} \quad (2)$$

where $\mathbf{g}(\mathbf{r}, t)$ is the gravitational acceleration vector, \mathbf{r}_s is the position of the Sun, and $p_s()$ is the solar radiation pressure, which varies with the distance to the Sun. The function $\mathbf{g}(\mathbf{r}, t)$ includes the main $1/r^2$ central force terms and higher-order spherical harmonic corrections that result from the Moon's non-spherical mass distribution. It also includes the effects of differences between the Earth's and the Sun's gravitational accelerations at the Moon's center of mass and at the spacecraft. $\mathbf{g}(\mathbf{r}, t)$ depends on the time t because of the attitude motion of the Moon with respect to MCIF coordinates and because of the motion of the Earth and the Sun relative to MCIF coordinates.

A first-order discrete-time Gauss-Markov process is used to model the dynamic variations of the acceleration disturbance:

$$\delta\mathbf{a}_{k+1} = e^{-\Delta t_k / \tau_{ak}} \delta\mathbf{a}_k + \sigma_{ak} \sqrt{1 - e^{-2\Delta t_k / \tau_{ak}}} \mathbf{v}_{ak} \quad (3)$$

This equation propagates between the sample times t_k and t_{k+1} , and $\Delta t_k = t_{k+1} - t_k$ is the sample interval. This Gauss-Markov process is driven by the three-dimensional discrete-time Gaussian white-noise sequence \mathbf{v}_{ak} , which has statistics $E\{\mathbf{v}_{ak}\} = 0$ and $E\{\mathbf{v}_{ak}\mathbf{v}_{ak}^T\} = I$. The first-order time constant of this process is $\tau_{ak} = \tau_{anom}[\|\mathbf{r}(t_k)\|/r_{anom}]^{1.5}$, and the target "steady-state" standard deviation of the process is $\sigma_{ak} = \sigma_{anom}[r_{anom}/\|\mathbf{r}(t_k)\|]^3$. τ_{anom} and σ_{anom} are nominal values for these quantities that apply when the spacecraft distance to the Moon's center takes on the nominal value $\|\mathbf{r}(t_k)\| = r_{anom}$. The altitude dependencies of τ_{ak} and σ_{ak} have been chosen roughly to reflect the types of variations that one might expect from modeling errors in the higher harmonics of the Lunar gravity model $\mathbf{g}(\mathbf{r}, t)$.

A discrete-time random walk is used to model the dynamic propagation of the solar radiation pressure parameter from time t_k to time t_{k+1} :

$$\beta_{k+1} = \beta_k + \sigma_\beta \sqrt{\Delta t_k} v_{\beta k} \quad (4)$$

The scalar discrete-time Gaussian white-noise sequence $v_{\beta k}$ drives this random walk. It has statistics $E\{v_{\beta k}\} = 0$ and $E\{v_{\beta k}^2\} = 1$. The intensity of the driving white noise is parameterized by σ_β .

The continuous-time differential equation model for the dynamics of $\mathbf{r}(t)$ and $\mathbf{v}(t)$ is transformed into a discrete-time model via numerical integration of the differential equations. This integration takes the usual form:

$$\mathbf{r}(t_{k+1}) = \int_{t_k}^{t_{k+1}} \mathbf{v}(\tau) d\tau \quad (5a)$$

$$\mathbf{v}(t_{k+1}) = \int_{t_k}^{t_{k+1}} \dot{\mathbf{v}}(\tau) d\tau = \int_{t_k}^{t_{k+1}} \left\{ \mathbf{g}[\mathbf{r}(\tau), \tau] + \frac{1}{2}[\delta\mathbf{a}_{k+1} + \delta\mathbf{a}_k] + \frac{1}{2}[\beta_{k+1} + \beta_k] p_s \left[\frac{\|\mathbf{r}(\tau) - \mathbf{r}_s(\tau)\|}{\|\mathbf{r}(\tau) - \mathbf{r}_s(\tau)\|} \right] \right\} d\tau \quad (5b)$$

Equation (5b) models the disturbance acceleration $\delta\mathbf{a}$ and the solar radiation pressure parameter β as being constants during the sample interval from t_k to t_{k+1} . These constants equal their average values over this interval.

Equations (3)-(5b) can be lumped into the generic discrete-time difference equation model form

$$\mathbf{x}_{k+1} = \mathbf{f}_k(\mathbf{x}_k, \mathbf{w}_k) \quad (6)$$

with \mathbf{x}_k and \mathbf{x}_{k+1} being the state vectors at the respective sample times t_k and t_{k+1} and \mathbf{w}_k being the discrete-time process-noise vector. It has four elements and is defined as follows:

$$\mathbf{w}_k = [\mathbf{v}_{ak}^T, \nu_{\beta k}]^T \quad (7)$$

It is a Gaussian white-noise process with statistics $E\{\mathbf{w}_k\} = 0$ and $E\{\mathbf{w}_k \mathbf{w}_k^T\} = I$.

A linearized version of the dynamics model in Eq. (6) is required by the EKF and the observability analysis. The linearized model uses the state-transition and disturbance-effectiveness Jacobian matrices

$$\Phi_k = \left. \frac{\partial \mathbf{f}_k}{\partial \mathbf{x}_k} \right|_{(\mathbf{x}_k, \mathbf{w}_k)} \quad \text{and} \quad \Gamma_k = \left. \frac{\partial \mathbf{f}_k}{\partial \mathbf{w}_k} \right|_{(\mathbf{x}_k, \mathbf{w}_k)} \quad (8)$$

Calculation of the \mathbf{r} and \mathbf{v} components of these matrices is carried out by integrating matrix differential equations. The required differential equations are derived in the usual way by differentiating the initial value problem associated with Eqs. (2), (5a), and (5b) with respect to its initial conditions in order to compute the \mathbf{r} and \mathbf{v} components of Φ_k or with respect to its forcing terms in order to compute the \mathbf{r} and \mathbf{v} components of Γ_k . Note that the computations implemented in the present study neglect the differentiation of the formulas for τ_{ak} and σ_{ak} with respect to \mathbf{r} because their dependence on \mathbf{r} has a negligible effect on Φ_k and Γ_k .

B. Measurement Model

The basic measurement of this system is the time that a star occults behind the Lunar limb or the time that a star rises from behind it. Let this time be called \tilde{t}^j , where j is the star catalog index of the star that occults or rises. A standard star camera would need software modifications in order to return measurements of \tilde{t}^j . The modified algorithm would look for non-occulted stars in the camera field of view (FOV) in order to determine the camera orientation, and it would identify all detected stars in its FOV. If a detected star disappeared without wandering off the edge of the FOV, then this disappearance would be deemed a Lunar occultation, and the time of the disappearance would be reported as \tilde{t}^j . Likewise, if any catalogued star suddenly appeared in the FOV without having entered it from the edge, then this appearance would be deemed a rising from behind the Lunar limb, and its time of appearance would be reported as \tilde{t}^j .

It is difficult to deal with time measurements in a Kalman filter because the filter uses time as the independent variable of its dynamic model. Therefore, it is preferable to model the occultation/rising time measurement in an altered form. A suitable transformation of the time measurement treats it as a measurement of the minimum Lunar altitude along the line-of-sight vector from the spacecraft to the star. This re-interpretation of the \tilde{t}^j measurement is depicted in Fig. 2. The figure depicts \mathbf{r}_{\min}^j as being the position vector of the minimum-altitude point along the unit-normalized line-of-sight (LOS) vector $\hat{\mathbf{r}}_s^j$ that points from the spacecraft position $\mathbf{r}(\tilde{t}^j)$ toward star j . The scalar α_{\min} is the distance from the spacecraft position to the minimum-altitude point.

Suppose that the star is far enough from the Moon so that parallax caused by orbital motion around the Moon is negligible. Under this assumption, the star direction $\hat{\mathbf{r}}_s^j$ as viewed from the spacecraft does not depend on the spacecraft position $\mathbf{r}(\tilde{t}^j)$.

coordinate system is the one in which λ and θ are defined. Given these quantities, it is possible to compute the Lunar altitude of any point along the LOS vector from the spacecraft to star j .

$$h^j(\alpha; \tilde{t}^j) = \left\| \mathbf{r}(\tilde{t}^j) + \alpha \hat{\mathbf{r}}_s^j \right\| - a_M[\lambda^j(\alpha; \tilde{t}^j), \theta^j(\alpha; \tilde{t}^j)] \quad (11)$$

where α is the distance of the point $\mathbf{r}(\tilde{t}^j) + \alpha \hat{\mathbf{r}}_s^j$ from the spacecraft and where $\lambda^j(\alpha; \tilde{t}^j)$ and $\theta^j(\alpha; \tilde{t}^j)$ are the Lunar longitude and latitude of this point. The longitude and latitude can be computed as follows:

$$\begin{bmatrix} r_{1M}^j(\alpha; \tilde{t}^j) \\ r_{2M}^j(\alpha; \tilde{t}^j) \\ r_{3M}^j(\alpha; \tilde{t}^j) \end{bmatrix} = A_M(\tilde{t}^j) [\mathbf{r}(\tilde{t}^j) + \alpha \hat{\mathbf{r}}_s^j] \quad (12a)$$

$$\lambda^j(\alpha; \tilde{t}^j) = \text{atan2}[r_{2M}^j(\alpha; \tilde{t}^j), r_{1M}^j(\alpha; \tilde{t}^j)] \quad (12b)$$

$$\theta^j(\alpha; \tilde{t}^j) = \text{asin}[r_{3M}^j(\alpha; \tilde{t}^j) / \left\| \mathbf{r}(\tilde{t}^j) + \alpha \hat{\mathbf{r}}_s^j \right\|] \quad (12c)$$

The altitude "measurement" for the high-fidelity model is computed by minimizing the altitude in Eq. (11) with respect to α :

$$y(\tilde{t}^j) = h_{\min}^j(\tilde{t}^j) + v_j = \min_{\alpha} [h^j(\alpha; \tilde{t}^j)] + v_j \quad (13)$$

As in Eq. (9), the actual "measured" value of the altitude is $y(\tilde{t}^j) = 0$. It is fairly straightforward to show that this altitude measurement model is equivalent to the simple spherical-Moon model in Eq. (9) under the assumption that the Lunar topography function is $a_M(\lambda, \theta) = a_{M0}$, a constant.

The altitude "measurement" error v_j is the result of three types of uncertainties. One type is a timing error in the star camera's determination of \tilde{t}^j . The second type of uncertainty is error in the star catalog's reported $\hat{\mathbf{r}}_s^j$ direction. The third type of uncertainty is error in the topographical map $a_M(\lambda, \theta)$. The net effect of these errors is assumed to be zero-mean Gaussian discrete-time white-noise so that v_j is Gaussian and has the statistics $E\{v_j\} = 0$ and $E\{v_j^2\} = \sigma_j^2$. The altitude "measurement" error standard deviation σ_j is modeled as being

$$\sigma_j = \sqrt{\sigma_h^2 + (\alpha_{\min} \sigma_s^j)^2 + (\dot{h}_{\min}^j \sigma_{tj})^2} \quad (14)$$

where σ_h is the RMS error in the Lunar topography map, σ_s^j is the per-axis standard deviation of the star catalog error in $\hat{\mathbf{r}}_s^j$, σ_{tj} is the RMS error in the measured occultation/rising time, and \dot{h}_{\min}^j is the time derivative of h_{\min}^j evaluated at $t = \tilde{t}^j$.

The timing error of the star camera in its measurement of \tilde{t}^j arises from two sources. The first source is the timing resolution of the star camera. The star camera determines \tilde{t}^j by comparing a star's measured light intensity against a threshold value. The time \tilde{t}^j is the time that star j 's intensity crosses the threshold value. The star camera needs to integrate received photons over a certain time interval in order to make a reliable determination of whether or not a star is present based upon its threshold value. The length of this time interval determines the camera's timing resolution. The second source of errors in the \tilde{t}^j measurement comes from edge diffraction of the starlight as it passes the Lunar limb. Edge diffraction smears out the light so that the illumination from the star takes a finite amount of time to decay from its nominal value to zero as the star sets behind the Moon¹⁶. The standard deviation of the edge-diffraction component of the timing error is approximately

$$\sigma_{tdiffj} = \frac{\left\| \mathbf{r}_{\min}^j \right\| \sqrt{\lambda_{light} \alpha_{\min}}}{(\mathbf{r}_{\min}^j)^T \mathbf{v}(\tilde{t}^j)} \quad (15)$$

where λ_{light} is the average wavelength of the star's light and the expressions involving r_{min}^j and $v(\tilde{t}^j)$ translate the Fresnel diffraction length scale term $\sqrt{\lambda_{light} \alpha_{min}}$ into an equivalent time by considering the speed with which the satellite crosses the plane that is tangent to the Moon at or near the point r_{min}^j . This error source can translate into position uncertainties on the order of 1 m for wavelengths of $\lambda_{light} = 5000$ Angstroms and for typical values of $\alpha_{min} = a_M$.

The errors in the topographic map $a_M(\lambda, \theta)$ and the errors in the reported star catalog directions \hat{r}_s^j are not really white noise. The same topographic error will recur if the same Lunar surface position (λ, θ) is the nearest point to the stellar LOS vectors of multiple star occultations/risings during a given filtering run. Similarly, the same star direction error will recur if the same star rises or sets more than once during a given run. Therefore, a filter that operates using the white-noise assumption for these error sources will be sub-optimal. There will be a large number of stars in a catalog and a large number of nearest surface points associated with occultations/risings. It is conjectured that these large numbers will produce sufficient randomness in the topography errors of unrelated surface points and in the star catalog errors of different stars to limit the impact of this departure from optimal filter design.

It is important to note that the star camera's angular resolution plays no role in determining the measurement error standard deviation σ_j . Attitude measurement uncertainty is the result of uncertainty about the center of a star's light as it is detected on the image plane of the star camera. The measurement of \tilde{t}^j is independent of which particular pixels detect the light from a particular star. The only important point is that the star camera must be able to identify whether or not it is detecting any light from the star in question. Similarly, the star camera's alignment uncertainty has no affect on σ_j .

There are two factors that will cause a practical star camera not to return \tilde{t}^j values for all possible star occultations/risings that occur as viewed from the spacecraft. First, a star camera has a limited FOV. It will not be able to detect occultations/risings for stars that lie outside its FOV. The second limiting factor is a star camera's inability to operate in glare. If the Sun or the sunlit portion of the Moon's surface lies in its FOV, then the resulting glare would interfere with camera operations and prohibit the camera from returning \tilde{t}^j values. Perhaps even glare from the Earth would preclude the measurement of occultation/rising times.

C. Filter Sampling at Regular Intervals

A special issue for this system is the randomness of the star occultation/rising sample times. One way to implement a Kalman filter for this system would be to sort the star occultation/rising times into an ascending sequence $\tilde{t}^{j_1} < \tilde{t}^{j_2} < \tilde{t}^{j_3} < \dots$ and to perform one dynamic propagation between each pair of times in the sequence and one measurement update at each successive sample time of the sequence. This approach can be inefficient if there are many star occultations/risings because the average time interval between occultations/risings might be too small for meaningful dynamic variations to occur over a given sample interval.

A more efficient approach is to use evenly spaced sample intervals such that $t_{k+1} - t_k = \Delta t_k = \Delta t$, a constant. A problem with this approach is that the star occultation times \tilde{t}^j normally will not coincide with the filter's measurement update times $t_k, t_{k+1}, t_{k+2}, \dots$. Therefore, additional modeling must be performed in this case in order to define a sensible measurement function.

The disparity between star occultation/rising times \tilde{t}^j and measurement update times t_k is resolved by using a spline to interpolate between the end times of a filter sample interval $[t_k, t_{k+1}]$. The spline is used to develop a measurement model that allows a simultaneous measurement update involving all star occultations/risings that occur during the given interval.

The following is an implementation of the required measurement model: Suppose that $\tilde{t}^{j_1}, \dots, \tilde{t}^{j_{m_k}}$ are the star occultation/rising times that lie within the filter sample interval $(t_k, t_{k+1}]$, i.e., $t_k < \tilde{t}^{j_i} \leq t_{k+1}$ for all $i = 1, \dots, m_k$. The following cubic spline formulas can be used to interpolate the satellite's position and velocity between the sample times t_k and t_{k+1} in order to determine these quantities at the star occultation/rising times $\tilde{t}^{j_1}, \dots, \tilde{t}^{j_{m_k}}$:

$$\begin{aligned}
\tilde{\mathbf{r}}_k(\tilde{t}^{j_i}) = & \mathbf{r}(t_k) \left[1 - 3 \left(\frac{\tilde{t}^{j_i} - t_k}{t_{k+1} - t_k} \right)^2 + 2 \left(\frac{\tilde{t}^{j_i} - t_k}{t_{k+1} - t_k} \right)^3 \right] + \mathbf{r}(t_{k+1}) \left[3 \left(\frac{\tilde{t}^{j_i} - t_k}{t_{k+1} - t_k} \right)^2 - 2 \left(\frac{\tilde{t}^{j_i} - t_k}{t_{k+1} - t_k} \right)^3 \right] \\
& + \mathbf{v}(t_k)(\tilde{t}^{j_i} - t_k) \left[1 - 2 \left(\frac{\tilde{t}^{j_i} - t_k}{t_{k+1} - t_k} \right) + \left(\frac{\tilde{t}^{j_i} - t_k}{t_{k+1} - t_k} \right)^2 \right] \\
& + \mathbf{v}(t_{k+1})(\tilde{t}^{j_i} - t_k) \left[- \left(\frac{\tilde{t}^{j_i} - t_k}{t_{k+1} - t_k} \right) + \left(\frac{\tilde{t}^{j_i} - t_k}{t_{k+1} - t_k} \right)^2 \right] \text{ for } i = 1, \dots, m_k
\end{aligned} \tag{16a}$$

$$\begin{aligned}
\tilde{\mathbf{v}}_k(\tilde{t}^{j_i}) = & \frac{\mathbf{r}(t_k)}{t_{k+1} - t_k} \left[-6 \left(\frac{\tilde{t}^{j_i} - t_k}{t_{k+1} - t_k} \right) + 6 \left(\frac{\tilde{t}^{j_i} - t_k}{t_{k+1} - t_k} \right)^2 \right] + \frac{\mathbf{r}(t_{k+1})}{t_{k+1} - t_k} \left[6 \left(\frac{\tilde{t}^{j_i} - t_k}{t_{k+1} - t_k} \right) - 6 \left(\frac{\tilde{t}^{j_i} - t_k}{t_{k+1} - t_k} \right)^2 \right] \\
& + \mathbf{v}(t_k) \left[1 - 4 \left(\frac{\tilde{t}^{j_i} - t_k}{t_{k+1} - t_k} \right) + 3 \left(\frac{\tilde{t}^{j_i} - t_k}{t_{k+1} - t_k} \right)^2 \right] \\
& + \mathbf{v}(t_{k+1}) \left[-2 \left(\frac{\tilde{t}^{j_i} - t_k}{t_{k+1} - t_k} \right) + 3 \left(\frac{\tilde{t}^{j_i} - t_k}{t_{k+1} - t_k} \right)^2 \right] \text{ for } i = 1, \dots, m_k
\end{aligned} \tag{16b}$$

The interpolated position $\tilde{\mathbf{r}}_k(\tilde{t}^{j_i})$ from Eq. (16a) can be used in Eqs. (10a) and (10b) in place of $\mathbf{r}(\tilde{t}^{j_i})$ order to determine α_{\min} and $\mathbf{r}_{\min}^j(\mathbf{x})$, and the norm of the latter quantity can be used in Eq. (9) in order to compute the modeled altitude measurement. The interpolated velocity $\tilde{\mathbf{v}}_k(\tilde{t}^{j_i})$ from Eq. (16b) can be used in place of $\mathbf{v}_k(\tilde{t}^{j_i})$ in the time derivatives of Eqs. (10a), (10b), and (9). These derivatives are needed to compute $\dot{h}_{\min}^j(\tilde{t}^j)$, which in turn is used in Eq. (14) to compute σ_j .

The resulting interpolated measurement model takes the non-standard form

$$0 = \mathbf{y}_k = \mathbf{h}_k(\mathbf{x}_k, \mathbf{x}_{k+1}) + \mathbf{v}_k \tag{17}$$

where $\mathbf{h}_k(\mathbf{x}_k, \mathbf{x}_{k+1})$ is the m_k -dimensional function that gives the modeled minimum altitudes along the LOS vectors to the occulting/rising stars and \mathbf{v}_k is the m_k -dimensional zero-mean Gaussian white-noise measurement error vector. The m_k -by- m_k square-root information matrix for \mathbf{v}_k is R_{v^k} , and $R_{v^k}^{-1} = \text{diag}(\sigma_{j_1}, \dots, \sigma_{j_{m_k}})$. This model is non-standard because its "measurement" \mathbf{y}_k is known a priori to equal 0 and because its modeled measurement function $\mathbf{h}_k(\mathbf{x}_k, \mathbf{x}_{k+1})$ depends on the state at two sample times. The a priori knowledge of \mathbf{y}_k is the result of the transformation from time measurements to altitude "measurements". The functional dependence of $\mathbf{h}_k(\mathbf{x}_k, \mathbf{x}_{k+1})$ is a direct result of the use of the interpolation in Eq. (16a) to compute the spacecraft positions at the occulting/rising times that occur during the sample interval from t_k to t_{k+1} -- recall that the $\mathbf{r}(t_k)$ and $\mathbf{v}(t_k)$ vectors in Eq. (16a) are elements of \mathbf{x}_k and that the $\mathbf{r}(t_{k+1})$ and $\mathbf{v}(t_{k+1})$ vectors are elements of \mathbf{x}_{k+1} .

The EKF and the observability analysis require a linearized model of the measurements in Eq. (17). This linearized model uses the following two Jacobian matrices: $H_{1k} = \partial \mathbf{h}_k / \partial \mathbf{x}_k$ and $H_{2k} = \partial \mathbf{h}_k / \partial \mathbf{x}_{k+1}$. Each row of these Jacobians can be computed via differentiation of the corresponding spline formula in Eq. (16a), differentiation of Eqs. (10a), (10b), and (9), and application of the chain rule.

III. An EKF in SRIF form and a Linearized Observability Calculation

The design of the EKF and the observability analysis of its state vector both rely on a non-standard form of the extended SRIF calculations. The basic difference from the standard linear SRIF calculations of ¹⁷ is that the dynamic propagation and the measurement update are performed simultaneously. This non-standard approach is needed because of the presence of states at two sample times in the Eq. (17) measurement model.

A. Nonstandard Extended SRIF

The SRIF stores a state estimate and a square-root information matrix. It uses these quantities to form a state information equation that models its uncertainty as follows:

$$\hat{R}_{xxk}(\mathbf{x}_k - \hat{\mathbf{x}}_k) = -\hat{\mathbf{v}}_{xk} \quad (18)$$

where \hat{R}_{xxk} is the filter's square-root information matrix and $\hat{\mathbf{x}}_k$ is its state estimate at sample time t_k . The discrete-time Gaussian white-noise sequence $\hat{\mathbf{v}}_{xk}$ models the filter's estimation error. The modeled statistics of $\hat{\mathbf{v}}_{xk}$ are $E\{\hat{\mathbf{v}}_{xk}\} = 0$ and $E\{\hat{\mathbf{v}}_{xk}\hat{\mathbf{v}}_{xk}^T\} = I$. The overstrike (^) on the quantities in Eq. (17) indicate that they correspond to the filtered estimate, which is also known as the a posteriori estimate. This usage differs from preceding sections, where the overstrike (^) signifies a unit vector in 3-space, as in $\hat{\mathbf{r}}_s^j$. Equation (18) can be used to show that the estimation error's covariance matrix is $\hat{P}_{xxk} = \hat{R}_{xxk}^{-1} \hat{R}_{xxk}^T$.

The combined dynamic propagation and measurement update for the sample interval $[t_k, t_{k+1}]$ uses Eq. (6) linearized about $\mathbf{x}_k = \hat{\mathbf{x}}_k$ and $\mathbf{w}_k = 0$ and Eq. (17) linearized about $\mathbf{x}_k = \hat{\mathbf{x}}_k$ and $\mathbf{x}_{k+1} = \bar{\mathbf{x}}_{k+1} = \mathbf{f}_k(\hat{\mathbf{x}}_k, 0)$. Its calculations are:

$$\bar{\mathbf{x}}_{k+1} = \mathbf{f}_k(\hat{\mathbf{x}}_k, 0) \quad (19a)$$

$$Q_{k+1} \begin{bmatrix} \hat{R}_{wwk} & \hat{R}_{wxk} \\ 0 & \hat{R}_{xxk+1} \\ 0 & 0 \end{bmatrix} = \begin{bmatrix} I & 0 \\ -\hat{R}_{xxk} \Phi_k^{-1} \Gamma_k & \hat{R}_{xxk} \Phi_k^{-1} \\ -R_{vvk} H_{1k} \Phi_k^{-1} \Gamma_k & R_{vvk} (H_{1k} \Phi_k^{-1} + H_{2k}) \end{bmatrix} \quad (19b)$$

$$\hat{\mathbf{x}}_{k+1} = \bar{\mathbf{x}}_{k+1} + [0 \ \hat{R}_{xxk+1}^{-1} \ 0] Q_{k+1}^T \begin{bmatrix} 0 \\ 0 \\ -R_{vvk} \mathbf{h}_k(\hat{\mathbf{x}}_k, \bar{\mathbf{x}}_{k+1}) \end{bmatrix} \quad (19c)$$

These equations are used to compute the filtered (i.e., a posteriori) state estimate $\hat{\mathbf{x}}_{k+1}$ and the corresponding square-root information matrix \hat{R}_{xxk+1} . Orthonormal/upper-triangular (QR) factorization¹⁸ of the large block matrix on the right-hand side of Eq. (19b) is used to compute the matrices on the left-hand side of Eq. (19b). The square matrix Q_{k+1} is orthonormal, and the square matrices \hat{R}_{wwk} and \hat{R}_{xxk+1} are upper-triangular. The identity matrix in the upper left-hand entry of the block matrix on the right-hand side of Eq. (19b) constitutes the a priori R_{ww} matrix. If the third row in the block matrix on the right-hand side of Eq. (19b) were dropped, then the equation would compute the a priori square-root information matrix \bar{R}_{xxk+1} in place of \hat{R}_{xxk+1} . The third row of the matrix and the corresponding non-zero third row of the vector on the right-hand side of Eq. (19c) constitute the measurement update terms in this formulation. At the end of these calculations, the filter has completed its computations for the sample interval from t_k to t_{k+1} , and it is ready to begin its calculations for the sample interval from t_{k+1} to t_{k+2} .

B. Linearized Observability/Constructability Calculations in SRIF Form

Calculations similar to those of the preceding sub-section have been used in order to compute the constructability Gramian of the linearized system. Recall that the constructability Gramian is like the observability Gramian. If it is full rank, then the system is constructible, which means that its final state can be estimated purely from the measurement outputs of the given interval over which the constructability Gramian has been computed. If the system's state transition matrix is non-singular, which is the case for the current system, then constructability is equivalent to observability. Thus, the constructability Gramian can be used in order to evaluate the system's observability.

SRIF-like calculations can be used to compute a square-root of a re-normalized constructability Gramian. The resulting matrix is the square-root information matrix for the error in the filtered estimate of \mathbf{x}_k under the assumptions of zero a priori information about \mathbf{x}_0 and zero process noise. In effect, this is the square-root information matrix of a batch-type filter. Let this matrix be called \tilde{R}_{xxk} . It is computed as follows:

$$\tilde{R}_{xx0} = 0 \quad (20a)$$

$$\tilde{Q}_{k+1} \begin{bmatrix} \tilde{R}_{xxk+1} \\ 0 \end{bmatrix} = \begin{bmatrix} \tilde{R}_{xxk} \Phi_k^{-1} \\ R_{vvk} (H_{1k} \Phi_k^{-1} + H_{2k}) \end{bmatrix} \quad \text{for } k = 0, \dots, K-1 \quad (20b)$$

where the computation of the square, upper-triangular matrix \tilde{R}_{xxk+1} and the square orthonormal matrix \tilde{Q}_{k+1} on the left-hand side of Eq. (20b) is accomplished via QR factorization of the block matrix on the right-hand side. Equation (20a) initializes the calculation, and Eq. (20b) is a recursion that propagates the square-root information matrix forward in time, much like Eq. (19b) for the SRIF filter calculations. These calculations can use the same Φ_k , H_{1k} and H_{2k} matrices as are used by the filter in its linearizations of Eqs. (6) and (17).

The system's constructability Gramian is the symmetric matrix $\tilde{R}_{xxK}^T \tilde{R}_{xxK}$. The system is constructible (and observable) if and only if this Gramian is full-rank. An equivalent constructability (and observability) condition is that the corresponding batch-like covariance matrix $\tilde{P}_{xxK} = \tilde{R}_{xxK}^{-1} \tilde{R}_{xxK}^{-T}$ has all finite entries. The matrix \tilde{P}_{xxK} gives a good indication of the degree of constructability (and observability). The square roots of its diagonal elements give an indication of the batch filter accuracy for the corresponding state vector element. If any of them are very large, then the constructability (and the observability) are poor. If any of them are infinite, then the system is not constructible (nor is it observable).

IV. Truth-Model Simulation

A truth-model simulation has been developed in order to produce simulated star occultation/rising times and simulated "truth" orbital states. Its simulated measurements have been filtered using the EKF of Section III, and the EKF state estimates have been compared with the "truth" states in order to evaluate this system's likely performance.

Several issues have been explored using the truth-model simulation. The two most significant questions concern uncertainties in the gravity model and in the Lunar topography, and the impact of these uncertainties on orbit determination accuracy. Gravitational uncertainty has been introduced by using slightly different spherical harmonic models in the truth-model simulation and the filter. Various levels of uncertainty in the Lunar topographic map have been simulated by adding random occultation time errors to the measured occultation times. The sizes of these errors are consistent with various levels of RMS altitude error in the Lunar map. Borrowing from Eq. (14), the standard deviation of the simulated timing uncertainty is

$$(\sigma_{ij})_{sim} = \sqrt{\sigma_h^2 / (h_{min}^j)^2 + \sigma_{ij}^2} \quad (21)$$

This standard deviation is larger than the timing standard deviation σ_{ij} , which is due to camera time resolution and starlight edge diffraction, because this timing uncertainty also includes the topography error effects through σ_h .

The filter uses a slightly different star catalog than the truth-model simulation. The differences between the direction vectors \hat{r}_s^j of the two catalogs implement the uncertainty that is modeled by the star catalog error standard deviation σ_s^j . This modeling approach eliminates the need for a σ_s^j component in the random part of the truth-model measurement error, which is why Eq. (21) differs from Eq. (14) through its lack of a σ_s^j term.

The simulation has used both randomly generated and real star catalogs. These two options have been used in order to study whether the actual distribution of useable stars has an impact on this system's performance.

The truth-model has been used to assess the impact of practical limitations of star camera technology by simulating a spacecraft that carries a number of star cameras, each of which has a limited FOV. The cameras are distributed angularly around the spacecraft yaw axis and are canted at a fixed tilt angle toward the Lunar limb in a way that should produce a significant number of occultation/rising measurements along the mission's nominal orbit. Only Lunar star occultations and risings that occur within the FOV of a star camera can be detected. No measurement is recorded if the camera sees too much of the Moon, and consequently too few reference stars to correctly identify the occulted star. Additionally, no occultation is detected if the camera in question is blinded by a source of glare, such as the Sun, the sunlit side of the Moon, or the Earth. By discarding measurements from the

entire camera if a source of glare is detected, this simulation is conservative because real star cameras are equipped with baffles to block light from one region of the camera FOV while still using other regions.

If a camera FOV is too wide, then the camera is more likely to be blinded by glare, but if it is too small, then it will not see much of the Lunar limb. Ideally, the spacecraft would have many small-FOV cameras, but the use of two or three medium-FOV cameras is more realistic.

For a given number of cameras, the simulation can be used to determine an optimal FOV size and tilt angle to see the greatest number of occultations over the greatest fraction of the orbit. Highly elliptical orbits would be a challenge for this system because, during much of the orbit, the spacecraft would be too close and see only the Lunar surface, or it would be too far away and see only the sky. If a given mission will have a highly elliptical orbit, then the designer can compensate by using additional star cameras and by tilting them at different angles, so that at least one camera will always be oriented toward the Lunar limb. For a circular orbit, a common fixed tilt angle for all cameras is optimal.

V. Observability and Filtering Results

A. Observability

The constructability Gramian of Eqs. (20a) and (20b) has been computed for a number of scenarios. It has been demonstrated to have full rank and to be well conditioned after differences in variable scalings are compensated. These properties prove that the system is constructible and, because its state transition matrix is invertible, that the system is also observable.

Care must be taken not to use too long of an interval for the constructability calculation. Suppose that the interval is very long compared to the acceleration disturbance Markov process time constant from Eq. (3), τ_{ak} . Then the constructability calculations will overflow the computer's ability to store large numbers. This overflow happens because Φ_k^{-1} in the recursion of Eq. (20b) has eigenvalues whose magnitudes are too much larger than 1, and the many iterations of Eq. (20b) result in too much growth and eventually lead to numerical overflow.

B. Filter Performance Results

The performance of this system is illustrated by a representative example. The satellite's orbit in this example is nearly circular with an altitude of $315 \text{ km} \pm 0.5 \text{ km}$, an inclination of 89.9° , and an orbital period of 8344 s . The star catalog contains the 2000 brightest stars. The spacecraft is assumed to carry three star cameras separated by 120° in yaw and tilted downward from local level by 33.3° . The RMS error between the filter's gravity model and that of the truth-model simulation is $1 \times 10^{-5} \text{ m/s}^2$ along the orbit. This error is optimistic for current gravity models, which have an accuracy level of $1 \times 10^{-4} \text{ m/s}^2$ to $3 \times 10^{-4} \text{ m/s}^2$ (10-30 mGal) on the near side of the Moon, and which are less accurate on the far side¹⁹. However, several missions in the near future, including the Japanese SELENE mission and NASA's Lunar Reconnaissance Orbiter, will improve gravity model accuracy^{13,19,20,21}, and other proposed missions hope to achieve gravity accuracy of $1 \times 10^{-5} \text{ m/s}^2$ or greater¹⁵. The truth-model simulation's error standard deviation for the Lunar topographic model is $\sigma_h = 100 \text{ m}$ RMS, and its error standard deviation for the star tracker timing is $\sigma_t = 1 \text{ ms}$. This level of σ_h map error is very optimistic at the present, particularly on the far side of the Moon, but it will be much more reasonable after the planned Lunar Reconnaissance Orbiter mission has completed its laser altimetry survey¹⁴. The filter tuning parameters that have been used in this run are:

$$\tau_{ak} = (10 \text{ s}) \times [||\mathbf{r}_k|| / (1.83 \times 10^6 \text{ m})]^{1.5}, \quad \sigma_{ak} = (1 \times 10^{-5} \text{ m/s}^2) \times [(1.83 \times 10^6 \text{ m}) / ||\mathbf{r}_k||]^3, \quad (22a)$$

$$\sigma_\beta = 4.7 \times 10^{-5} \text{ m}^2 / (\text{kg} \cdot \text{s}^{0.5}), \quad \sigma_h = 100 \text{ m}, \quad \text{and} \quad \sigma_t = 0.001 \text{ s} \quad (22b)$$

The position and velocity estimation results for this filter run are depicted in Figs. 3 and 4. Although the initial position error is more than 10 km, the filter converges to steady-state in less than three orbits, its peak position component error after three orbits is less than 70 m (Fig. 3), and its peak velocity component error is less than 0.045 m/s after the third orbit (Fig. 4). The actual errors are consistent with the filter's computed standard deviations, as evidenced by the rough correspondence between the actual errors (the solid curves on Figs. 3 and 4) and their computed standard deviations (the thin dotted curves on Figs. 3 and 4).

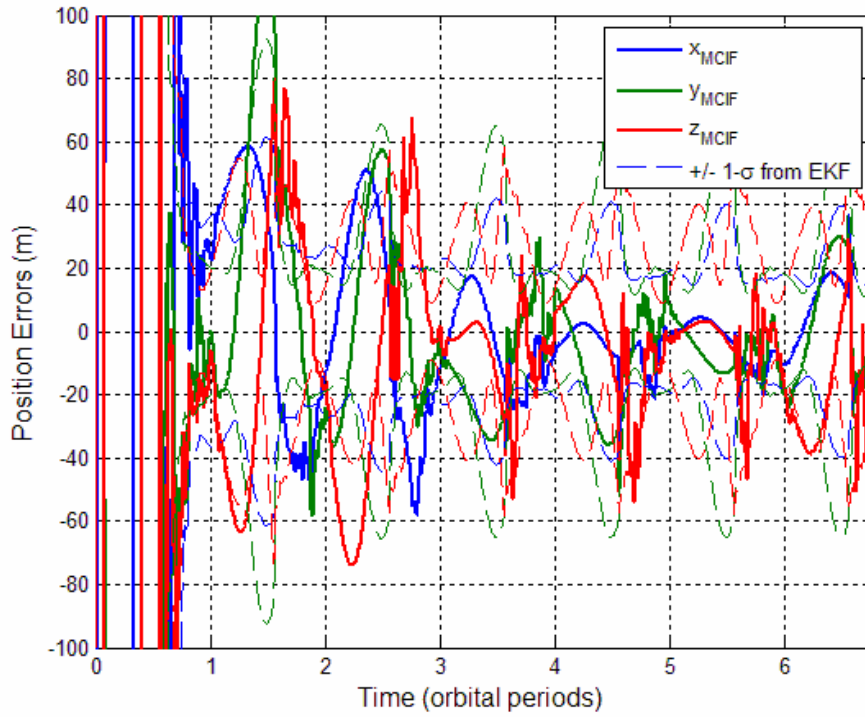


Figure 3. Position error time histories for a representative filter run when operating on data from a truth-model simulation.

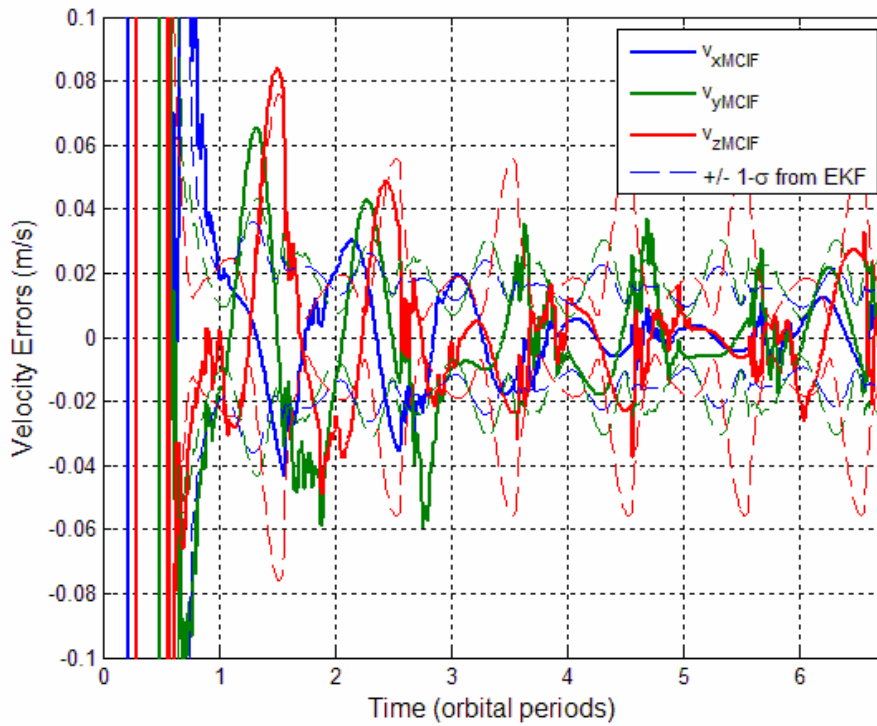


Figure 4. Velocity error time histories for a representative filter run when operating on data from a truth-model simulation.

Figure 5 compares the orbit's altitude time history (top plot) with its distribution of sensed star occultations/risings (bottom plot). The vertical scale of the top plot indicates that the orbit is nearly circular. The bottom plot shows a dot whenever the star whose catalog number is given on the vertical scale sets behind or rises above the Lunar limb within a camera FOV that is not blinded by glare. The gaps between the clouds of dots occur when the spacecraft is passing over the sunlit side of the Moon.

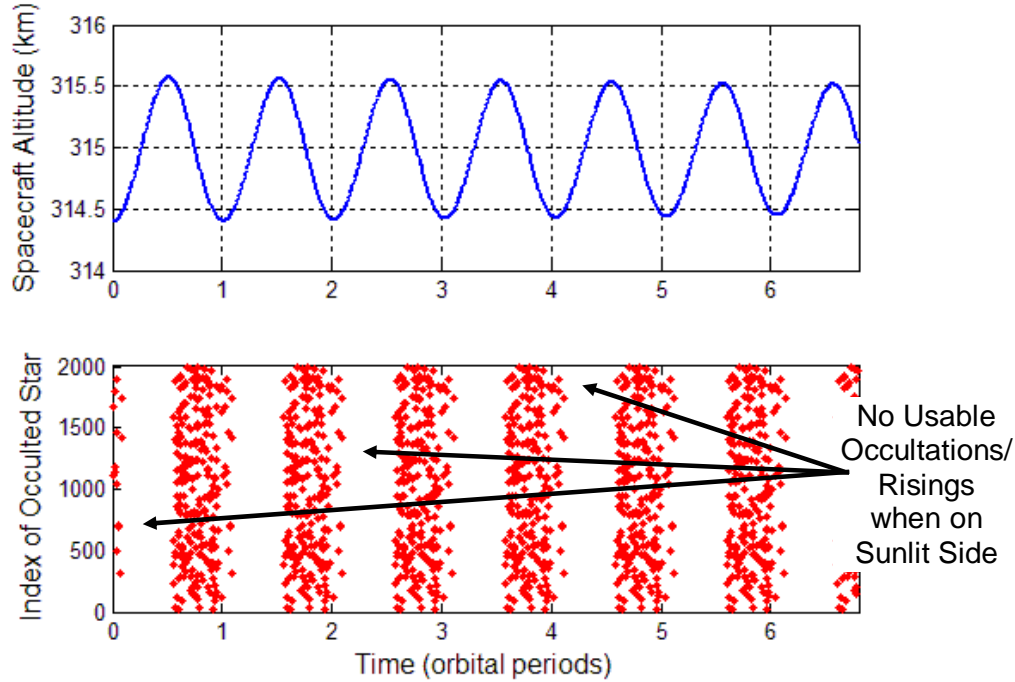


Figure 5. Altitude time history and distribution of occultations/risings for a representative filter run when operating on data from a truth-model simulation.

A comparison between the lower panel of Fig. 5 and Figs. 3 and 4 illustrates the effect of data availability on the system's accuracy. Consider the periods when data gaps occur on the sunlit side of the Moon during the intervals from $t = 0.1$ to 0.5 orbits, from $t = 1.1$ to 1.5 orbits, from $t = 2.1$ to 2.5 orbits, and so on. The filter's computed σ values tend to grow when the cameras are blinded by glare from the sunlit side of the Moon, and they tend to decrease during the intervening intervals, when data again become available. Thus, the system tends to drift when occultation/rising data are sparse or completely unavailable, but the system very quickly recovers accuracy after a period of data unavailability has ended. As a result of this behavior, the fraction of the orbit over which occultations/risings are visible is more critical than their sheer number. It is noteworthy that the peak position errors are significantly less than the assumed RMS Lunar topographic map errors ($\sigma_h = 100$ m). This fact indicates that the filter is able to exploit the accuracy of its dynamic model in order to achieve a certain amount of averaging of the topographic errors. The extent to which this averaging occurs depends on the relative magnitudes of the topographic and gravitational error components, or to put it in general estimation terms, on the relative accuracy of the measurement model and the dynamic model.

The following are three significant trends of the simulation results: First, the system's accuracy and convergence robustness tend to degrade in highly elliptical orbits that use a limited number of star cameras with fixed pointing directions relative to the spacecraft's nominally nadir-pointing body frame. This fact is thought to be the result of the greatly reduced number of occultation/rising measurements that are available in such a configuration. Second, errors in the star catalog have a relatively small effect on orbit determination accuracy for values of σ_s^j consistent with currently available catalogs. Third, no significant performance difference has been found between a randomly simulated star catalog and an actual star catalog if the catalog contains a sufficient number of the brightest stars (i.e., 500-2000). Therefore, it is concluded that the actual star catalog covers a sufficient portion of the sky to support the operations of this system in a nearly optimal manner.

VI. Summary and Conclusions

A new system for autonomous Lunar orbit determination has been proposed and analyzed. Its basic measurements are the times of occultations and risings of stars as their LOS vectors graze the Lunar limb. These occultation/rising times can be measured using a modified star camera. They give position information by locating the spacecraft on a cylinder that is tangent to the Moon and that extends along the known LOS direction to the star.

The system's basic observability has been verified by performing a numerical observability/constructability analysis of a linearized model, and an extended Kalman filter has been developed for this system. This filter has been tested using a truth-model simulation. The Kalman filter exhibits good convergence robustness, and it can achieve a steady-state absolute position accuracy with a peak per-axis error of 70 m if it has access to a Lunar topographic map with an RMS error of 100 m or less and if it has a Lunar gravity model that has an RMS error of $1 \times 10^{-5} \text{ m/s}^2$ (1 mGal). System accuracy tends to increase with increased availability of occultation/rising measurements, which can be achieved by using a large star catalog in conjunction with a wide-angle star camera equipped to block excess light, or in conjunction with an array of narrow-angle star cameras.

References

- ¹Hill, K., Parker, J., Born, G.H., and Demandante, N., "A Lunar L₂ Navigation, Communication, and Gravity Mission," AIAA Paper No. 2006-6662, *Proc. AIAA/AAS Astrodynamics Specialists Conf.*, 21-24 Aug. 2006, Keystone, CO.
- ²Chory, M.A., Hoffman, D.D., and LeMay, J.L., "Satellite Autonomous Navigation -- Status and History," *Proc. IEEE Position, Location, and Navigation Symposium*, Las Vegas, NV, Nov. 4-7, 1986, pp. 110-121.
- ³Tai, F. and Noerdlinger, P.D., "A Low Cost Autonomous Navigation System", AAS Paper 89-001, *Guidance and Control 1989; Proc. Annual Rocky Mountain Guidance and Control Conf.*, Feb. 1989, Keystone, Colorado, pp. 3-23.
- ⁴Hicks, K.D., and Wiesel, W.E. Jr., "Autonomous Orbit Determination System for Earth Satellites," *Journal of Guidance, Control, and Dynamics*, Vol. 15, No. 3, May-June 1992, pp. 562-566.
- ⁵Lillestrand, R.L., Carroll, J.E., "Dynamic Space Navigation Employing Star Occultation Technique," U.S. Patent No. 3,360,638, Dec. 1967.
- ⁶Naqvi, A.M. "Satellite Navigation by Terrestrial Occultations of Stars I: General Considerations Neglecting Atmospheric Refraction and Extinction," Geophysics Corporation of America, Technical Report No. 62-18-A, Bedford, MA, Oct. 1962.
- ⁷Lillestrand, R.L., and Carroll, J.E., "Horizon-Based Satellite Navigation Systems," *IEEE Transactions on Aerospace and Navigational Electronics*, Vol. 10, No. 3, Sept. 1963, pp 247-270.
- ⁸Farrell, E.J., "Accuracy of Star Occultation Measurements for Satellite Navigation," *IEEE Transactions on Aerospace and Electronic Systems*, Vol. 3, No. 4, July 1967, pp. 643-655.
- ⁹Lillestrand, R.L., Hilt, W.M., Harrington, D.C., "Method and Apparatus for Occultation Detection for Space Navigation," U.S. Patent No. 3,274,880, Sept. 1966.
- ¹⁰Yunfeng, D. and Renwei, Z., "Stellar Sensor-Based Automatic Satellite Navigation," National Air Intelligence Center, Rept. NAIC-ID(RS)T-0311-96, 1996.
- ¹¹Silva, R.M., Jorris, T.R., and Vallerie, E.M. III, "Experiment D005 D-5: Star Occultation Navigation," NASA N68-14163, March 1967.
- ¹²Keenan, R.V., Regenhardt, J.D., "Star Occultation Measurements as an Aid to Navigation in CIS-Lunar Space," M.S. Dissertation, Dept. of Aeronautics and Astronautics, MIT, Cambridge, MA, 1962.
- ¹³Anon. "SELENE: The Moon," available on-line at <http://www.isas.ac.jp/e/enterp/missions/selene/index.shtml>, Jan. 2007.
- ¹⁴Keller, J., "The Lunar Reconnaissance Orbiter -- Instrument Suite and Measurements," available on-line at <http://lunar.gsfc.nasa.gov/library/keller51906.pdf>, Jan. 2007.
- ¹⁵Psiaki, M.L., "Absolute Orbit and Gravity Determination using Relative Position Measurements Between Two Satellites," to be presented at the *AIAA Guidance, Navigation, and Control Conf.*, Hilton Head, SC, Aug. 20-23, 2007.
- ¹⁶Lipson, S.G., Lipson, H., and Tannhauser, D.S., *Optical Physics, 3rd edition*, Cambridge Univ. Press, (Cambridge, UK, 1995), pp. 152-173.
- ¹⁷Bierman, G.J., *Factorization Methods for Discrete Sequential Estimation*, Academic Press, (New York, 1977), pp. 69-76, 115-122.
- ¹⁸Gill, P.E., Murray, W., and Wright, M.H., *Practical Optimization*, Academic Press, (New York, 1981), pp. 37-40.
- ¹⁹Smith, D.E., and Zuber, M.T., "Precision Orbit Determination of Low Altitude Lunar Spacecraft with Laser Systems," 14th Int'l. Laser Ranging Workshop, San Fernando, Spain, 6-11 June 2004. available on-line at http://cddis.nasa.gov/lw14/docs/presnts/sci6b_dsp.pdf.
- ²⁰Hupp, E., and Brown, D., "NASA Announces Discover Program Selections," available on-line at <http://stardust.jpl.nasa.gov/news/status/061030.html>, Oct. 2006.
- ²¹Spencer, H., Kekez, D.D., Zee, R.E., Carroll, K.A., Arkani-Hamed, J., "Lunette: Lunar Gravity Mapping with a Nanosatellite," *ASTRO 2006 – 13th CASI Canadian Astronautics Conference*, CASI, Ottawa, Ontario, 2006.